

Supporting Information

Flower-like Amorphous Metal-Organic-Frameworks-Based Hybrid-Solid-State

Electrolyte for High-performance Lithium-Metal Battery

Mingjie Liu^a, Zhongteng Chen^a, Bin Chen^a, Tengfei Liu^a, Pucheng Zhao^a, Junling Xu^a,

*Lianyi Shao^a, Xiaoyan Shi,^{*a} and Zhipeng Sun^{*a}*

*Corresponding authors

^a School of Materials and Energy, Guangdong University of Technology, Guangzhou,

Guangdong, P. R. China. E-mail: shixy222@gdut.edu.cn; zpsunxj@gdut.edu.cn

Table of contents

- 1. Experimental section**
- 2. Electrochemical measurements**
- 3. Supplementary information for schemes, figures and tables**

References

CRedit authorship contribution statement

1. Experimental section

Materials and chemicals: Copper (II) nitrate hydrate ($\text{Cu}(\text{NO}_3)_2 \cdot 3\text{H}_2\text{O}$, 98%), Phosphonitrilic chloride trimer(99%), Ethylparaben (98.0%), Triethylamine (THF,99.0%), N, N-Dimethylformamide (DMF, 99.8%) Ethanol (99.9%), Lithium bis(trifluoromethane) sulfonimide (LiTFSI, 99.9%) were all purchased from Macklin Reagent. Lithium iron phosphate (LFP), Carbon black (super-P), Polyvinylidene fluoride (PVDF), and N-methyl-2-pyrrolidone (NMP, 99.5%) were purchased from Aladdin Chemical Co., Ltd. Lithium foil was obtained from China Energy Lithium Co., Ltd. All chemicals were used directly without further purification. Deionized water was utilized throughout the experiments.

Synthesis of Cu-MOF and Cu-aMOF: The ligand hexa(4-carboxyphenoxy) cyclotriphosphazene (HCTP-COOH) was synthesized following a published procedure. The Cu-MOF was prepared under high pressure using a solvothermal method. For Cu-aMOF, solvothermal synthesis was conducted at atmospheric pressure. Typically, HCTP-COOH (0.4 mmol) and trihydrate copper (II) nitrate (1.2 mmol) were dissolved in 80 mL of dimethylformamide (DMF) and heated at 160°C for 2 h. The product was collected by centrifugation (8,000 rpm), washed with DMF and methanol several times, and dried at 120°C under vacuum for 24 h to yield blue powders.

Synthesis of Cu-MOF@Li and Cu-aMOF@Li: Cu-MOF and Cu-aMOF (350 mg each) were activated at 120°C under vacuum for 12 hours to expose unsaturated metal sites. The activated MOFs were then suspended in a 1 M LiTFSI/PC solution, yielding a bright-blue suspension. After stirring uniformly for 6 h, the products were collected by centrifugation and washed with pure PC solution. Finally, Cu-MOF@Li and Cu-aMOF@Li were obtained by drying in an oven at 100°C for 12 h.

Fabrication of MPIE and AMPIE: Typically, PVDF-HFP ($M_w \frac{1}{4} 350\ 000$) was dissolved in DMF and stirred for 6 hours to get a clear solution, the mass ratio of PVDF-

HFP: DMF was kept at 3: 40. Then the as-synthesized Li@MOFs, Li-IL (1 M LiTFSI in [EMIM]TFSI solution) and PVDF-HFP/DMF solution were added and sonicated for 24 h with a different mass ratio of 50%, 60%, 70%, and 80% to get a homogeneous solution. The percentages of Cu-MOF/Li-IL in the composite solid polymer electrolytes were designed to be 25%, 50%, 75%, and 1(mg VS. μL). Among them, those with a content of 70% and 75% were named as AMPIE (Cu-aMOF based) and MPIE (Cu-aMOF based), the others were named as “Li-IL content-Li@MOFs content” such as 0.5-70%, 0.5-80%, respectively. After that, the slurry was cast on a petri dish to volatilize the solvent at room temperature and was further heated at 60 °C under vacuum for 12 h to remove the residual solvent. The prepared electrolytes were then pressed into 16 mm discs, stored in a glove box, and used for battery assembly.

Assembly of Cells: The LiFePO_4 cathode was obtained by coating an NMP-based slurry containing 80 wt.% LiFePO_4 powder, 10 wt.% Super-C carbon, and 10 wt.% PVDF onto an aluminum foil. The mass loading of LiFePO_4 was controlled at about 2.0 to 2.5 mg with a diameter of 12 mm, lithium foil with a diameter of 15.6 mm was used as the anode. And the All cells were assembled in an Ar-filled glovebox ($\text{O}_2 < 0.1$ ppm, $\text{H}_2\text{O} < 0.1$ ppm). And the voltage window for battery testing is from 2.4 V to 4.0 V.

2. Electrochemical measurements

Ionic conductivity measurements of the SSEs were conducted using AC impedance spectroscopy using symmetric cells with blocking stainless-steel electrodes. The EIS measurements were performed over a temperature range of 20 to 80 °C, applying a 10 mV amplitude and a frequency range from 0.1 Hz to 100 kHz. The ionic conductivity is calculated using equation:

$$\sigma = \frac{L}{RA} \quad (1)$$

where L is the thickness of the SSEs, R is the bulk resistance of the SSEs measured by

EIS, and A is the area of the stainless-steel electrode. And the migration activation energy (E_a) was calculated using the Arrhenius equation:

$$\ln \sigma = \ln A - \frac{E_a}{RT} \quad (2)$$

where σ is the ionic conductivity, A is the pre factor, R is the molar gas constant ($R=8.314\text{J mol}^{-1} \text{K}^{-1}$), and T is the absolute temperature. The t_{Li^+} was determined by conducting DC polarization (DVDC: 10 mV) and AC impedance spectroscopy measurements on a symmetric Li//SE//Li cell. The t_{Li^+} values were calculated using the Bruce-Vincent equation:

$$t_{\text{Li}^+} = \frac{I_{\text{ss}}(\Delta V_{\text{DC}} - I_0 R_{\text{int},0})}{I_0(\Delta V_{\text{DC}} - I_{\text{ss}} R_{\text{int},\text{ss}})} \quad (3)$$

where I_0 and I_{ss} are the initial and steady-state currents, respectively, and $R_{\text{int},0}$ and $R_{\text{int},\text{ss}}$ are the initial and steady-state interface resistances of the electrolyte, respectively. Symmetric cells were assembled by sandwiching the AMPIE and MPIE electrolytes between two pieces of Li metal to investigate the performance of Li plating-stripping on the Li anode at the current densities of 0.1 mA cm^{-2} . The electrochemical stability windows of the AMPIE and MPIE were analyzed using LSV by sandwiching the SPEs between an Li reference and counter electrode, and a stainless-steel working electrode at a scan rate of 0.1 mV s^{-1} from open circuit voltage to 6 V.

4. Supplementary information for schemes, figures and tables

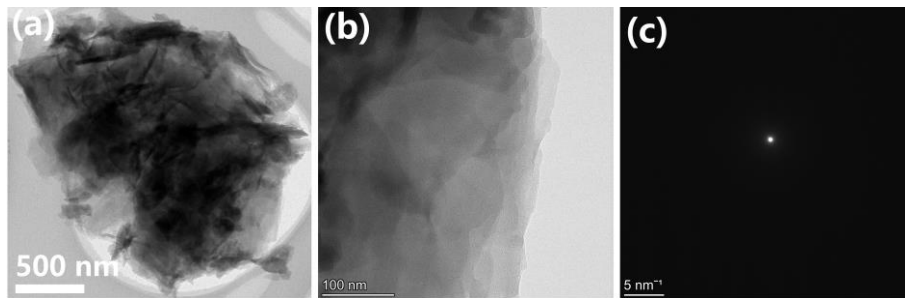


Fig. S1 (a) and (b) TEM images, and (c) SAED pattern of Cu-aMOF.

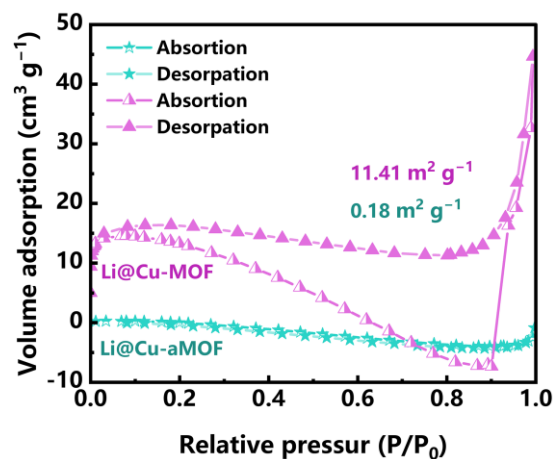


Fig. S2 N₂ adsorption isotherm of Li@Cu-MOF and Li@Cu-aMOF.

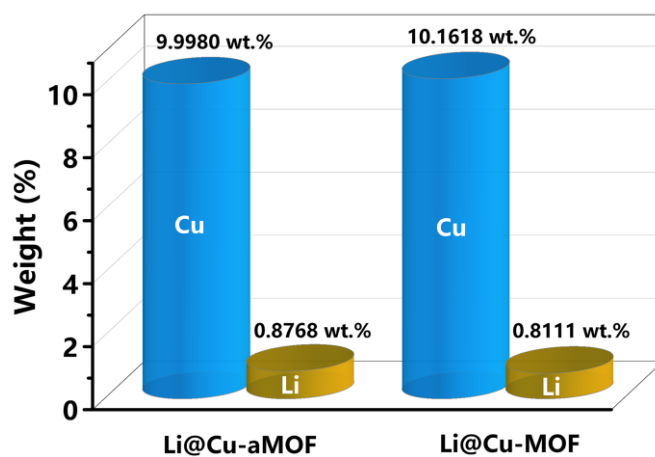


Fig. S3 ICP results of the Li@Cu-MOF and Li@Cu-aMOF.

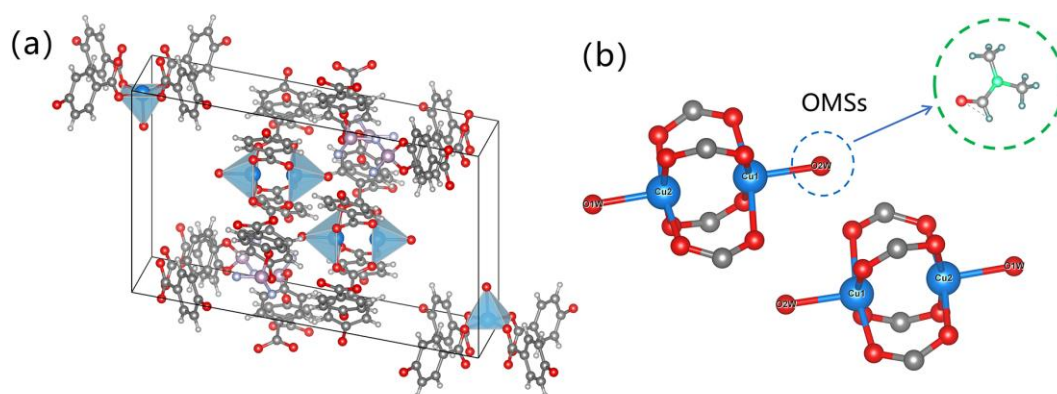


Fig. S4 Crystal Structure of Cu-MOF. (a) cell structure, and (b) Coordination environment of Cu²⁺ within the Cu-MOF.

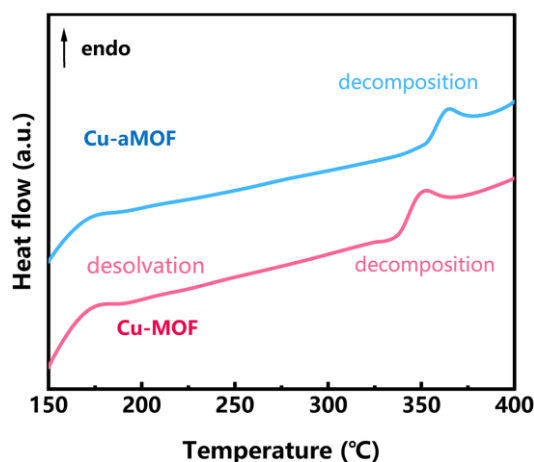


Fig. S5 The differential scanning calorimetry (DSC) upscan curves of Cu-MOF and Cu-aMOF in nitrogen atmosphere at $10\text{ }^{\circ}\text{C min}^{-1}$.

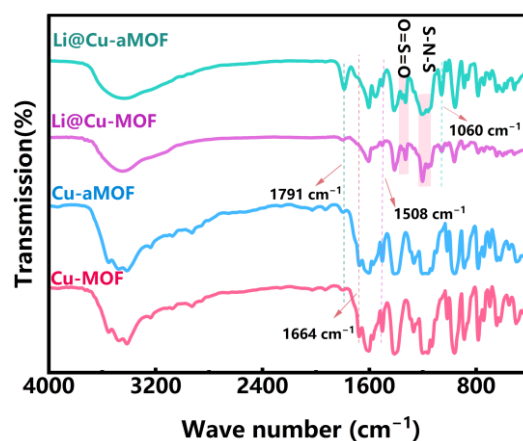


Fig. S6 Infrared spectrum of MOFs and Li@MOFs powders.

Both Cu-MOFs and Cu-aMOFs exhibit similar characteristic peaks, indicating that the MOFs synthesized via different approaches share the same structural framework, including chemical bonding and functional group profiles. Notably, characteristic absorption peaks at approximately 1610 cm^{-1} and 1410 cm^{-1} , corresponding to the coordinated carboxylic groups within the framework backbone, were observed. Additionally, peaks at approximately 1664 cm^{-1} and 1508 cm^{-1} , attributed to the stretching vibrations of C=O and C-N in DMF, were present, consistent with the TGA results. Following lithium salt incorporation, the DMF-related peaks weakened, accompanied by the emergence of new characteristic absorption peaks at 1791 cm^{-1} and 1060 cm^{-1} in the FT-IR spectra of Li@Cu-aMOF and Li@Cu-MOF, corresponding to the C=O and C-O-C stretching vibration of PC adsorbed within the framework.

Meanwhile, absorption peaks for O=S=O and S-N-S of TFSI⁻ anions were observed at approximately 1202 cm⁻¹ and 1328 cm⁻¹, respectively. These findings suggest that the DMF molecules coordinated within the MOFs were replaced by TFSI⁻ anions and PC solvent molecules during the incorporation process. Furthermore, the characteristic peaks associated with PC and TFSI⁻ anions were notably stronger in Li@Cu-aMOF compared to Li@Cu-MOF. These results underscore the superior adsorptive properties of amorphous Cu-aMOF, attributed to its higher specific surface area, greater pore volume, and the abundance of unsaturated OMS sites. These features facilitate the incorporation of more LiTFSI and PC molecules, promoting lithium salt dissociation and enhancing Li-ion transport.

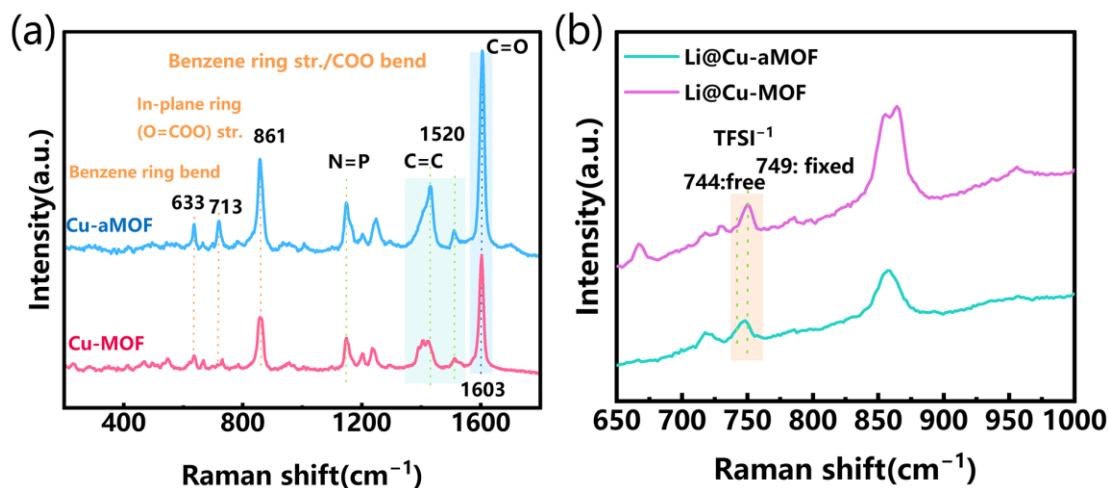


Fig. S7 Raman spectrum of (b) Cu-MOF and Cu-aMOF, and (c) Li@Cu-MOF and Li@Cu-aMOF.

Raman spectroscopy further corroborates these observations, with both Cu-aMOF and Cu-MOF exhibiting characteristic peaks of the HCTP-COOH ligand at 633, 713, 816, and 1194 cm⁻¹ (Fig. S7a). Fig. S7b highlights the interactions between TFSI⁻ anions and the MOFs, as evidenced by the shoulders at 744 and 749 cm⁻¹, corresponding to free and fixed TFSI⁻ anions, respectively.¹ Notably, Li@Cu-aMOF exhibited almost no free TFSI⁻ anions, while Li@Cu-MOF retained a small fraction. This suggests that the unsaturated metal sites in Cu-aMOF, with their localized electronic clouds, effectively promote the dissociation of lithium salts while securely anchoring TFSI⁻ anions through their acidic sites.

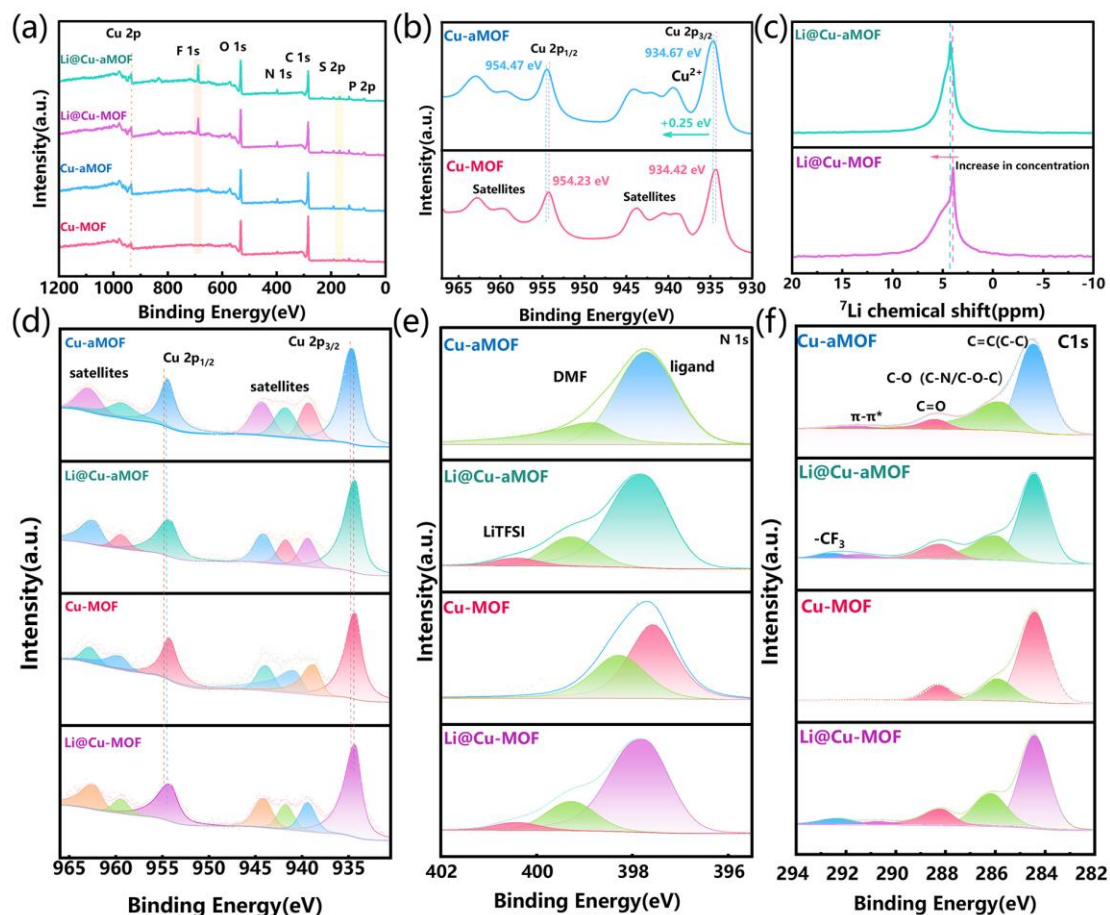
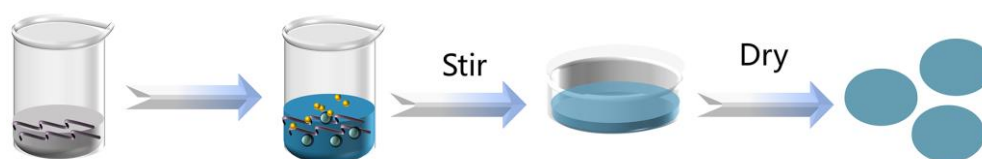


Fig. S8 X-ray Photoelectron Spectroscopy of (a) The full spectrum of Cu-MOF and Li@Cu-MOF powders, which displays the elements present in the sample, including C, N, O, F, P, Cu, and S, (b) High-resolution XPS analysis of the Cu 2p core-level emission from the Cu-MOF and Cu-aMOF, revealing the distinct spin-orbit split peaks of Cu 2p_{3/2} and Cu 2p_{1/2}. (c) Solid-state ⁷Li NMR spectrum of Li@MOFs. (d) High-resolution XPS analysis of the Cu 2p, (e) N 1s, and (f) C 1s.

As shown in Fig. S8a, elements integral to the MOFs (Cu, O, N, P) and extraneous elements associated with the Li@MOFs (F, S) were detected. High-resolution XPS spectra of Cu 2p (Fig. S8b) reveal the main peaks for Cu 2p_{1/2} and Cu 2p_{3/2} at binding energies around 934 eV and 954 eV, respectively, along with satellite peaks at higher binding energies. The similarity in Cu 2p peak profiles among the MOFs indicates that copper predominantly exists in the Cu²⁺ oxidation state, unaffected by crystallinity. Notably, Cu-aMOFs exhibit elevated binding energies for Cu²⁺ peaks compared to Cu-MOFs, indicating a lower electron cloud density around the central copper atoms. This

is attributed to the increased number of OMSs in Cu-aMOF, resulting from the removal of coordinated solvent molecules in the amorphous structure.² In the Li@MOFs (Fig. S8d), the negative shift in the binding energy of Cu 2p compared to the pristine MOFs suggests coordination between the unsaturated metal sites and dissociated TFSI⁻ anions. This shift in binding energy indicates that the electronegative TFSI⁻ anions interact with the active sites on the MOFs, altering the chemical environment of the copper centers. Such coordination enhances the ability of the MOFs to stabilize the dissociated TFSI⁻ anions, which, in turn, contributes to improved ionic conductivity and lithium-ion transport in the SSEs.³ The larger chemical shift from Cu-aMOF to Li@Cu-aMOF (Cu 2p_{3/2}: 954.47 eV to 954.14 eV) compared to that from Cu-MOF to Li@Cu-MOF (954.23 eV to 954.12 eV) is attributed to two factors: the higher OMSs density in Cu-aMOF and its greater adsorption capacity for LiTFSI.

This finding is further corroborated by the solid-state ⁷Li NMR spectra (Fig. S8c), which show a more pronounced negative shift and sharper peak for Li@Cu-aMOFs than Li@Cu-MOFs. This indicates greater Li⁺ ion freedom in Li@Cu-aMOFs due to its abundant PC solvent molecules and immobilized TFSI⁻ anions, which effectively promote LiTFSI dissociation. High-resolution XPS analysis of the N 1s and C 1s peaks (Fig. S8e & S8f) also confirms the presence of residual DMF molecules and the successful incorporation of LiTFSI salt in both Li@Cu-aMOFs and Li@Cu-MOFs.^{4, 5}



Scheme S1. The preparation process of an electrolyte membrane.

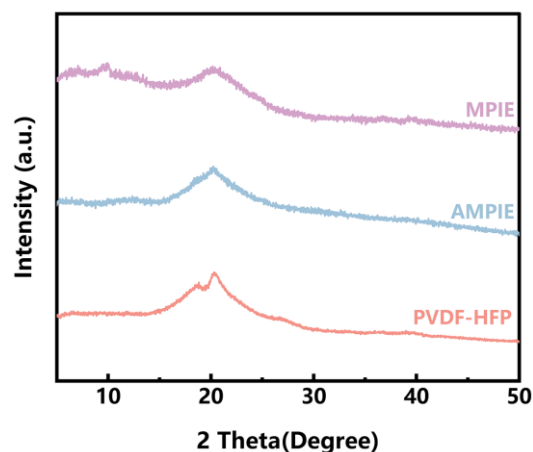


Fig. S9 XRD pattern of the synthesized AMPIE, MPIE, and PVDE-HFP film.

The PVDF-HFP sample was prepared by dissolving commercially obtained PVDF-HFP in dimethylformamide (DMF), followed by drying to form a film before XRD analysis. As shown in Fig. S9, the results reveal that pristine PVDF-HFP exhibits two broad peaks at approximately $2\theta = 20^\circ$, a characteristic feature of semi-crystalline polymers.⁶ This structural trait is also preserved in MOF-based electrolytes. Notably, the amorphous Cu-aMOF-based AMPIE displays an even broader peak than PVDF-HFP, suggesting that Cu-aMOF disrupts the polymer matrix ordering and increases the amorphous phase fraction. Additionally, a small broad peak at $2\theta = 9^\circ$ is observed in MPIE, attributed to the presence of Cu-MOF. The enhanced amorphous phase in both AMPIE and MPIE facilitates greater polymer chain segment mobility, which is advantageous for improving ion conductivity.

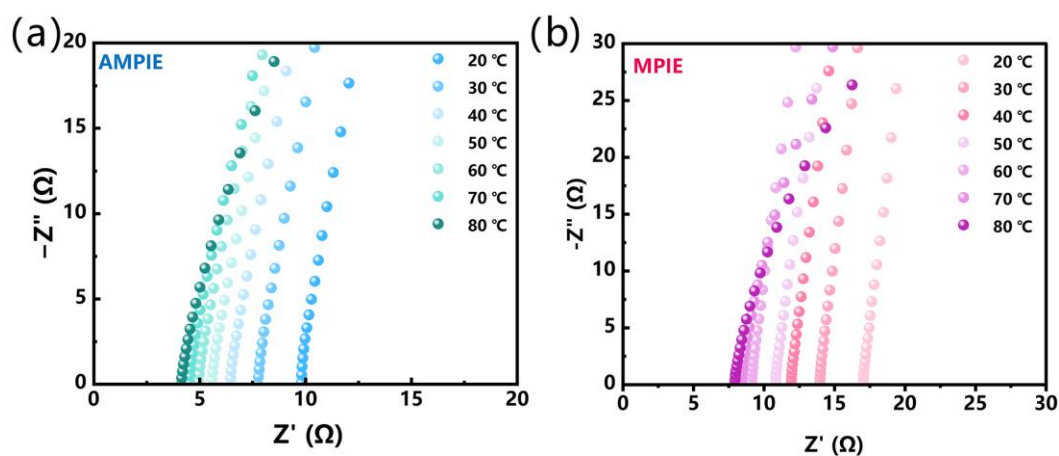


Fig. S10 Electrochemical impedance spectroscopy at different temperatures: (a) AMPIE and (b) MPIE

Table S1 Ionic conductivity of MPIE and AMPIE at different testing temperatures ranges from 20 °C to 80 °C.

Temperature	AMPIE	MPIE
20 °C	$1.36 \times 10^{-3} \text{ S cm}^{-1}$	$9.37 \times 10^{-4} \text{ S cm}^{-1}$
30 °C	$1.61 \times 10^{-3} \text{ S cm}^{-1}$	$1.18 \times 10^{-3} \text{ S cm}^{-1}$
40 °C	$1.87 \times 10^{-3} \text{ S cm}^{-1}$	$1.42 \times 10^{-3} \text{ S cm}^{-1}$
50 °C	$2.05 \times 10^{-3} \text{ S cm}^{-1}$	$1.65 \times 10^{-3} \text{ S cm}^{-1}$
60 °C	$2.23 \times 10^{-3} \text{ S cm}^{-1}$	$1.86 \times 10^{-3} \text{ S cm}^{-1}$
70 °C	$2.38 \times 10^{-3} \text{ S cm}^{-1}$	$2.04 \times 10^{-3} \text{ S cm}^{-1}$
80 °C	$2.51 \times 10^{-3} \text{ S cm}^{-1}$	$2.21 \times 10^{-3} \text{ S cm}^{-1}$

Table S2 Comparison of some reported solid-state electrolytes' conductivity and transference number.

Materials	Conductivity	Li ⁺ transference number	Ref.
LSN-MOF	$7.41 \times 10^{-4} \text{ S cm}^{-1}$	0.59	7
UN-LiM-EMIM	$3.0 \times 10^{-4} \text{ S cm}^{-1}$	0.338	8
PVDF-HFP/LLZO/ LiTFSI@UiO-66(F)	$4.9 \times 10^{-4} \text{ S cm}^{-1}$	0.51	9
HKUST@PIN-IL-Li	$4 \times 10^{-4} \text{ S cm}^{-1}$	0.367	10
MGM-MOF-OH	$7.1 \times 10^{-4} \text{ S cm}^{-1}$	0.81	11
MOF-BZN	$8.76 \times 10^{-4} \text{ S cm}^{-1}$	0.75	12
(PEO-n-UIO)	$1.3 \times 10^{-4} \text{ S cm}^{-1}$	0.35	13
Zn-MOF-74/Li-IL	$1.73 \times 10^{-4} \text{ S cm}^{-1}$	0.47	14
Li-IL@HKUST-1	$1.20 \times 10^{-4} \text{ S cm}^{-1}$	0.13	3
IUP _{1.8}	$4.3 \times 10^{-4} \text{ S cm}^{-1}$	0.45	15
Li-IL@MOF	$3.0 \times 10^{-4} \text{ S cm}^{-1}$	0.36	16
Li-ILs@HPCN	$1.91 \times 10^{-4} \text{ S cm}^{-1}$	0.5	17

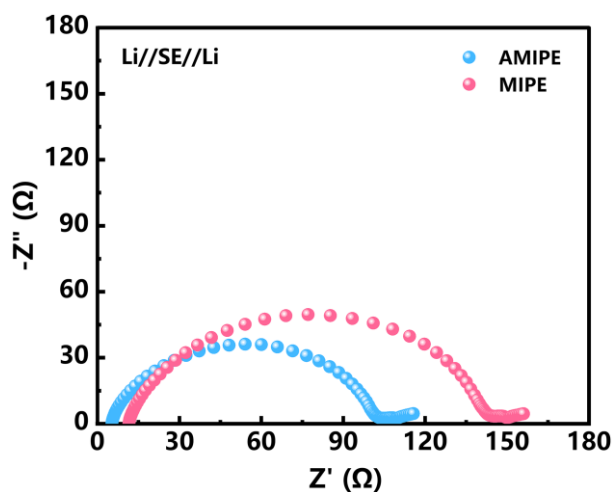


Fig. S11 Electrochemical impedance spectroscopy of symmetrical batteries.

The initial high-frequency impedance spectra reveal semicircles corresponding to the charge-transfer resistance (R_{ct}). AMPIE exhibits an R_{ct} of approximately 105 Ω , significantly lower than the 147 Ω observed for MPIE. This lower R_{ct} value indicates a more efficient charge transfer process and suggests that AMPIE forms a more stable and compatible interface with the lithium metal anode, further validating the superior electrochemical performance of the amorphous Cu-aMOF-based SSE.

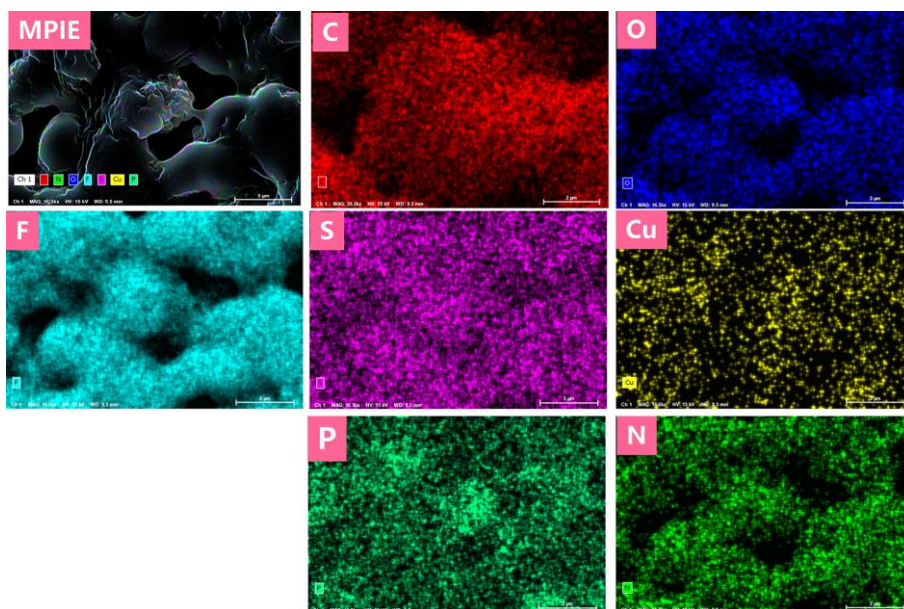


Fig. S12 Elemental mapping via energy-dispersive X-ray spectroscopy (EDS) of MPIE, with elements distribution of C, N, O, P, F, S, and Cu.

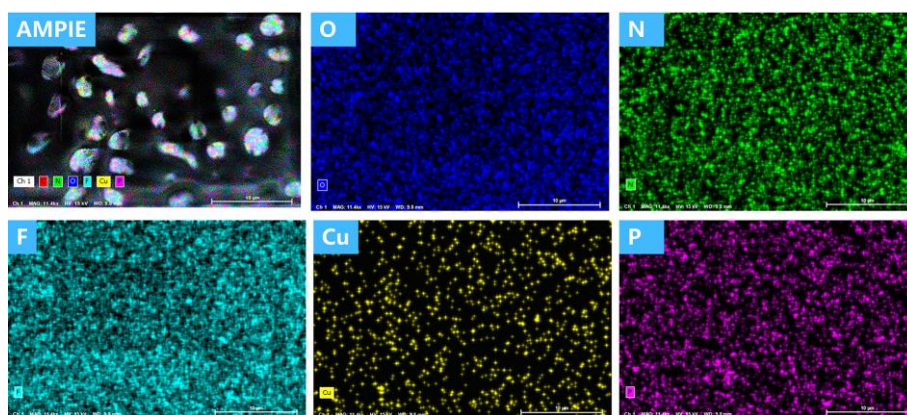


Fig. S13 Elemental mapping via energy-dispersive X-ray spectroscopy (EDS) of MPIE, with elements distribution of N, O, P, F, and Cu.

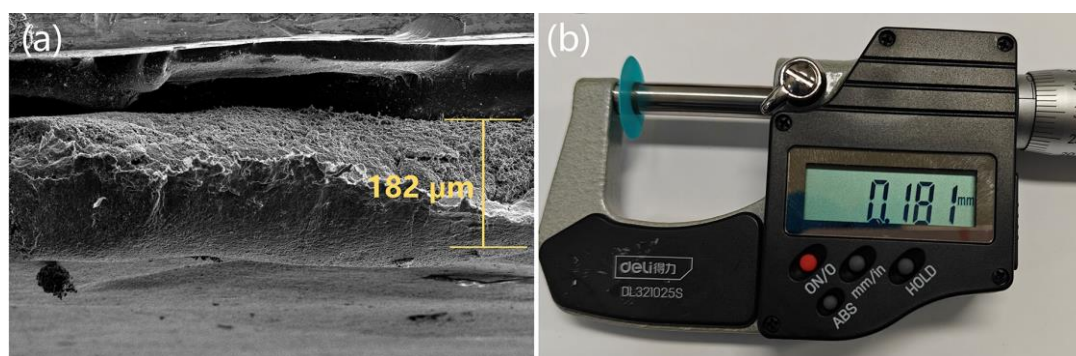


Fig. S14 Characterization of SSEs. (a) SEM image of cross-section, (b) Thickness of AMPIE.

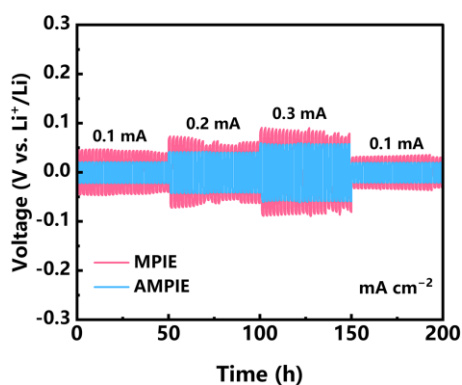


Fig. S15 Li-stripping cycling performance of Li//AMPIE//Li and Li//MPIE//Li at different densities of 0.1-0.3 mA cm⁻² for 200 h.

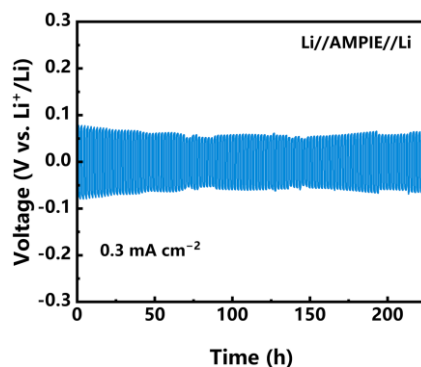


Fig. S16 Li-stripping cycling performance of Li//AMPIE//Li at 0.3 mA cm^{-2} .

Table S3 Comparison of plating/stripping results with the published reports.

Electrolyte	Current density (mA cm^{-2})	Stripping time (h)	WT ($^{\circ}\text{C}$)	Ref.
ZR8-7.5	0.1	8000	60	18
H-ZIF-8/HNT	0.1	1000	RT	19
UN-LiM-IL	0.1	1000	RT	8
HP-HK-0	0.1	1800	RT	20
HKUST@PIN-IL-Li	0.1	200	RT	10
15%Cu-MOF/P-Li	0.1	1080	60	21
PMSE	0.1	2000	RT	22
HKUST@PI/PVDF	0.1	900	30	23
CSPE	0.15	500	60	24
CPE-5	0.1	1300	60	25
AMPIE	0.1	4000	RT	This work

WT = working temperature, RT = room temperature

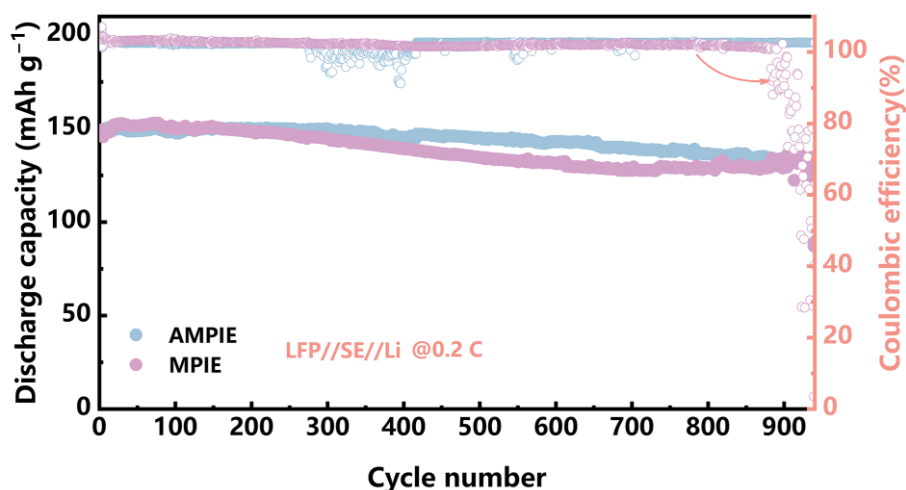


Fig. S17 The cycling performance of AMPIE and MPIE at 0.2 C, and the morphology of lithium metal anodes was obtained after cycling for 940 cycles in the two cells.

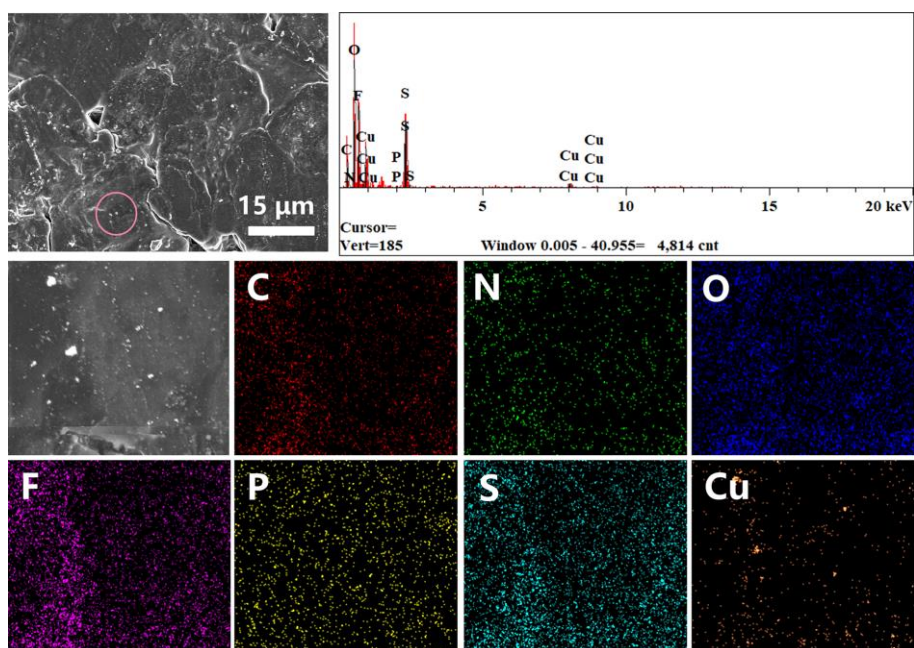


Fig. S18 Elemental mapping images of lithium anode surface after 940 cycles in LFP//AMPIE//Li cells.

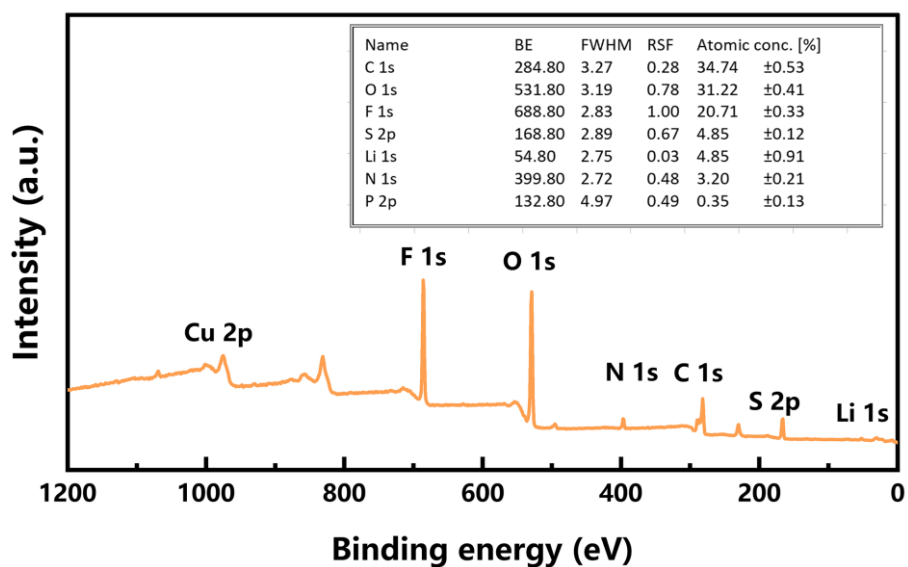


Fig. S19 The full XPS spectrum of the lithium anode reveals the surface composition and atomic content of the anode after cycling.

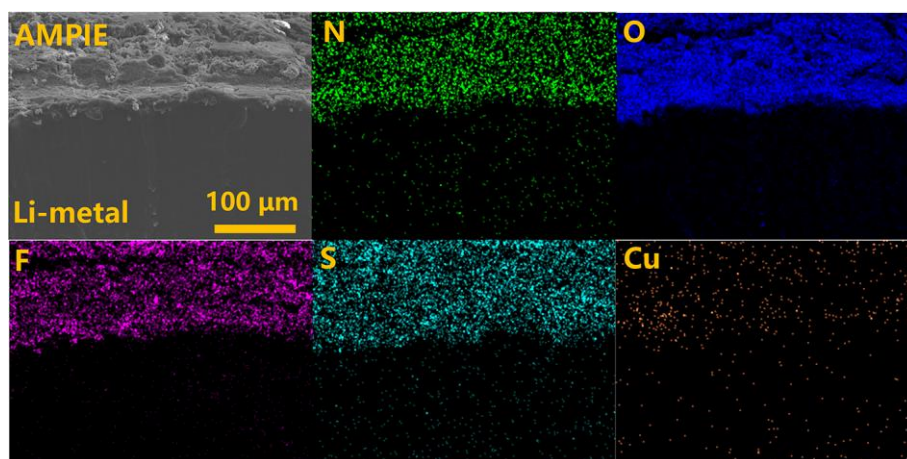


Fig. S20 Cross-sectional SEM images and SEM-EDS mapping of the interface of Li//AMPIE//Li cell after lithium plating-stripping at 0.1 mA cm^{-2} at room temperature for 2000 h.

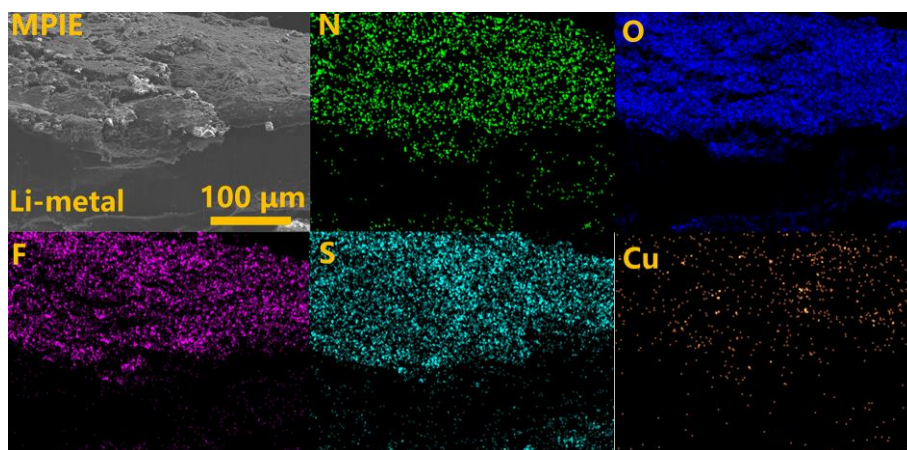


Fig. S21 Cross-sectional SEM images and SEM-EDS mapping of the interface of Li//MPIE//Li cell after lithium plating-stripping at 0.1 mA cm^{-2} at room temperature for 2000 h.

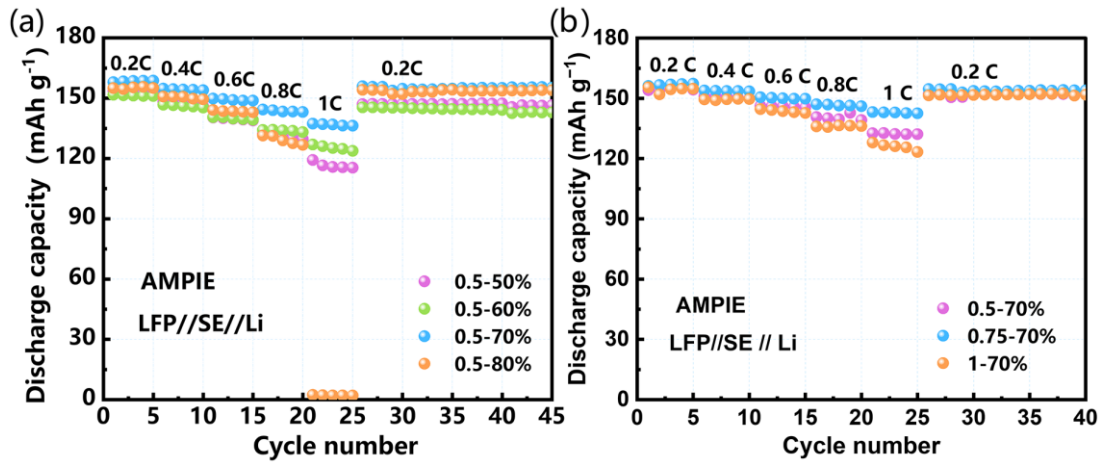


Fig. S22 Electrochemical performance of amorphous MOFs-based hybrid SSEs. Rate capability at the discharge rate of 0.2 C to 2 C ($1\text{ C} = 170\text{ mAh g}^{-1}$) of (a) different content of Cu-aMOF, and (b) different content of ionic liquids.

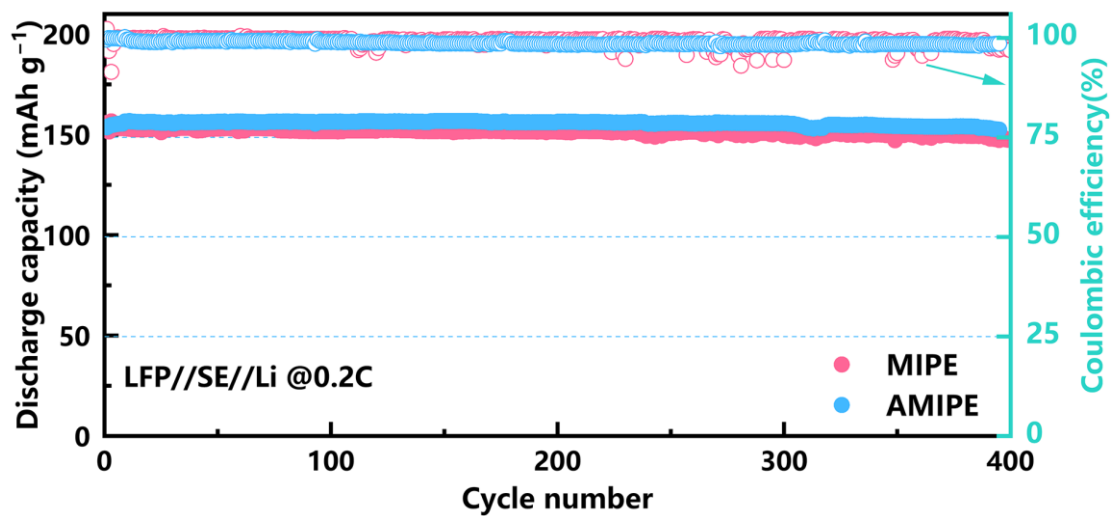


Fig. S23 The cycling performance of AMPIE and MPIPE at 0.2 C, room temperature.

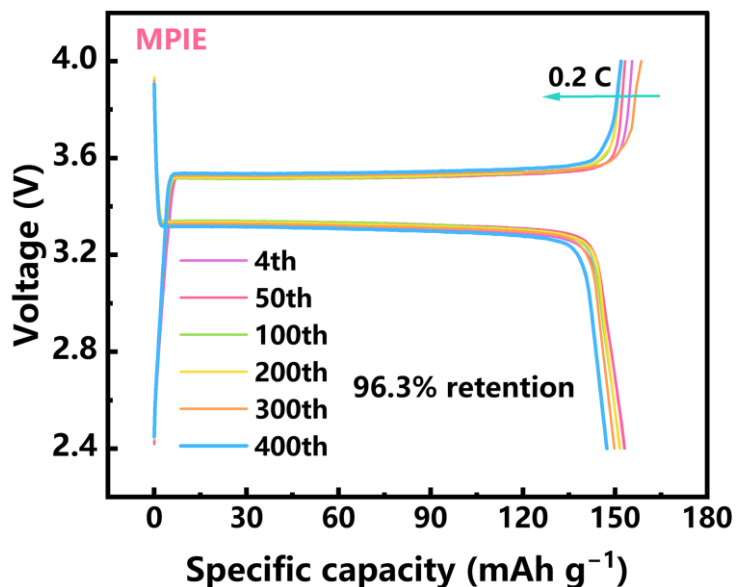


Fig. S24 Charge and discharge curves of MPIE at specific cycle numbers (4th, 50th, 100th, 200th, 300th, and 400th) at a 0.2C rate.

Table S4 Comparison of cycling performance of MOFs-based electrolytes with published reports

Materials	Cathode/Anode	Voltage range (V)	Initial capacity (mAh g ⁻¹)	Retention (%)	Temperature (°C)	Ref.
ZR8-7.5	LiFePO ₄ /Li	2.6-4.0	144.9 (0.5 C)	80.53% (800)	60	18
H-ZIF-8/HNT	LiFePO ₄ /Li	2.5-4.2	124 (1 C)	84% (200)	RT	19
UN-LiM-EMIM	LiFePO ₄ /Li	2.0-4.0	126 (1 C)	84.9% (350)	RT	8
HP-HK-0	LiFePO ₄ /Li	2.5-4.2	162.9 (0.1 C)	79% (150)	RT	20
MGM-MOF-OH	LiFePO ₄ /Li	2.5-4.0	~160 (0.2 C)	-(100)	30	11
LSN-MOF	LiFePO ₄ /Li	2.5-4.0	148.2 (0.2 C)	93.7% (200)	25	7
MOF-BZN	LiFePO ₄ /Li	2.5-4.0	~130 (0.5 C)	-(300)	30	12
Li-Cuboct-H	LiFePO ₄ /Li	2.4-4.0	117 (1 C)	93% (210)	30	26
PEO/L-5Z	LiFePO ₄ /Li	2.5-4.2	163.7 (0.2 C)	95% (100)	60	27

Li-MOF/PEO	LiFePO ₄ /Li	2.4-4.2	161 (0.5 C)	94.4% (300)	60	28
ZIF-67-LAPAM	LiFePO ₄ /Li	2.5-4.0	102.7 (10 C)	88.4% (1000)	30	29
AMPIE	LiFePO₄/Li	2.4-4.0	154.9 (0.2 C)	98.5% (400)	RT	This work

RT = room temperature

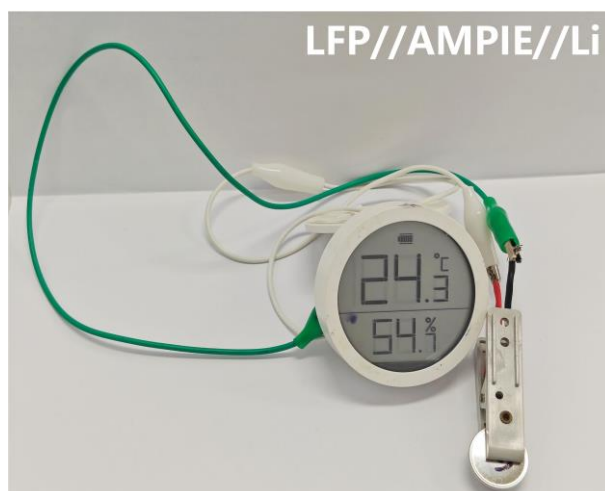


Fig. S25 Application illustration of LFP//AMPIE//Li cell.

References

- 1 N. Chen, Y. Li, Y. Dai, W. Qu, Y. Xing, Y. Ye, Z. Wen, C. Guo, F. Wu and R. Chen, *J. Mater. Chem. A*, 2019, **7**, 9530-9536.
- 2 C. W. Gao, Z. J. Jiang, S. B. Qi, P. X. Wang, L. R. Jensen, M. Johansen, C. K. Christensen, Y. F. Zhang, D. B. Ravnsbaek and Y. Z. Yue, *Adv. Mater.*, 2022, **34**, e2110048.
- 3 Z. T. Wang, H. Zhou, C. F. Meng, W. W. Xiong, Y. J. Cai, P. F. Hu, H. Pang and A. H. Yuan, *ACS Appl. Energy Mater.*, 2020, **3**, 4265-4274.
- 4 J. Zhu, S. He, H. Tian, Y. Hu, C. Xin, X. Xie, L. Zhang, J. Gao, S. M. Hao, W. Zhou and L. Zhang, *Adv. Funct. Mater.*, 2023, **33**, 2306060.
- 5 S. Park, J. Lee, B. Kim, C. Y. Jung, S. E. Bae, J. Kang, D. Moon and J. Park, *J. Am. Chem. Soc.*, 2024, **146**, 9293-9301.

- 6 J. Zhou, X. Wang, J. Fu, L. Chen, X. Wei, R. Jia and L. Shi, *Small*, 2023, **20**, e2309317.
- 7 T. Zhao, W. Kou, Y. Zhang, W. Wu, W. Li and J. Wang, *J. Power Sources*, 2023, **554**, 232349.
- 8 Z. Wu, Y. Yi, F. Hai, X. Tian, S. Zheng, J. Guo, W. Tang, W. Hua and M. Li, *ACS Appl. Mater.*, 2023, **15**, 22065-22074.
- 9 T. Wang, X. Zhang, N. Yuan and C. Sun, *Chem. Eng. J.*, 2023, **451**, 138819.
- 10 X. Tian, Y. Yi, Z. Wu, G. Cheng, S. Zheng, B. Fang, T. Wang, D. G. Shchukin, F. Hai, J. Guo and M. Li, *Chem. Eng. Sci.*, 2023, **266**, 118271.
- 11 Y. Xie, L. Xu, Y. Tong, Y. Ouyang, Q. Zeng, D. Li, Y. Xiao, S. Yu, X. Liu, C. Zheng, Q. Zhang and S. Huang, *Adv. Mater.*, 2024, **36**, e2401284.
- 12 Y. Ouyang, W. Gong, Q. Zhang, J. Wang, S. Guo, Y. Xiao, D. Li, C. Wang, X. Sun, C. Wang and S. Huang, *Adv. Mater.*, 2023, **35**, e2304685.
- 13 J.-F. Wu and X. Guo, *J. Mater. Chem. A*, 2019, **7**, 2653-2659.
- 14 P. Dong, X. Zhang, W. Hiscox, J. Liu, J. Zamora, X. Li, M. Su, Q. Zhang, X. Guo, J. McCloy and M. K. Song, *Adv. Mater.*, 2023, **35**, e2211841.
- 15 L. Liu and C. Sun, *ChemElectroChem*, 2020, **7**, 707-715.
- 16 Z. Wang, R. Tan, H. Wang, L. Yang, J. Hu, H. Chen and F. Pan, *Adv. Mater.*, 2018, **30**, 1704436.
- 17 Z. Zhang, Y. Huang, H. Gao, C. Li, J. Hang and P. Liu, *J. Energy Chem.*, 2021, **60**, 259-271.
- 18 S. Kim, H. Jamal, F. Khan, A. Al-Ahmed, M. M. Abdelnaby, A. Al-Zahrani, S.-E. Chun and J. H. Kim, *J. Mater. Chem. A*, 2024, **12**, 10942-10955.
- 19 F. C. Tao, X. Wang, S. Jin, L. Tian, Z. X. Liu, X. M. Kang and Z. L. Liu, *Adv. Mater.*, 2023, **35**, e2300687.
- 20 X. Wang, L. Tian, F. Tao, M. Liu, S. Jin and Z. Liu, *Dalton Trans.*, 2023, **52**, 10222-10230.
- 21 J. Wu, Y. Ma, H. Zhang, H. Xie, J. Hu, C. Shi, B. Chen, C. He and N. Zhao, *ACS Appl. Mater.*, 2024, **16**, 16351-16362.

- 22 L. Wei, X. Xu, K. Xi, X. Shi, X. Cheng, Y. Lei and Y. Gao, *ACS Appl. Mater. Interfaces*, 2024, **16**, 878-888.
- 23 S. Y. Zheng, Z. L. Li, L. Y. Chen, Y. T. Huang, J. K. Shi, S. X. Wang, Y. Liu, Y. Liu, Y. P. Cai and Q. F. Zheng, *ACS Mater. Lett.*, 2023, **5**, 1136-1144.
- 24 L. Wei, X. Xu, S. Jiang, K. Xi, L. Zhang, Y. Lan, J. Yin, H. Wu and Y. Gao, *J J. Colloid Interface Sci.*, 2023, **630**, 232-241.
- 25 H. Lian, R. Momen, Y. Xiao, B. Song, X. Hu, F. Zhu, H. Liu, L. Xu, W. Deng, H. Hou, G. Zou and X. Ji, *Adv. Funct. Mater.*, 2023, **33**, 2306060.
- 26 H. Liu, H. Pan, M. Yan, X. Zhang and Y. Jiang, *Adv. Mater.*, 2023, **35**, e2300888.
- 27 C. Li, S. Deng, W. Feng, Y. Cao, J. Bai, X. Tian, Y. Dong and F. Xia, *Small*, 2023, **19**, e2300066.
- 28 Z. Zhang, L. Tian, H. Zhang, H. Xu, P. Dong, Y. Zhang and D. Long, *AACS Appl. Energy Mater.*, 2022, **5**, 1095-1105.
- 29 J. Guan, X. Feng, Q. Zeng, Z. Li, Y. Liu, A. Chen, H. Wang, W. Cui, W. Liu and L. Zhang, *Adv. Sci. (Weinh)*, 2023, **10**, e2203916.

CRedit authorship contribution statement

Mingjie Liu: Investigation, Data curation, Methodology, Writing – original draft.
Zhongteng Chen: Investigation. Bin Chen: Investigation, Data curation. Tengfei Liu: Investigation. Pucheng Zhao: Investigation. Junling Xu: Data curation. Lianyi Shao: Data curation. Xiaoyan Shi: Supervision, Conceptualization, Methodology, Writing – original draft, Writing – review & editing, Funding acquisition, Zhipeng Sun: Validation, Supervision, Funding acquisition.